

# Validation of FEM models describing moisture transport in heated concrete by Magnetic Resonance Imaging

S.J.F. Erich <sup>(1)</sup>, A.B.M. v. Overbeek <sup>(1)</sup>, G.H.A. v.d. Heijden <sup>(2)</sup>, L. Pel <sup>(2)</sup>, H.P. Huinink <sup>(2)</sup>

W.H.A. Peelen <sup>(1)</sup> and A.H.J.M. Vervuurt <sup>(1)</sup>

(1) TNO Built Environment and Geosciences, Delft, The Netherlands; bart.erich@tno.nl

(2) Eindhoven University of Technology, Eindhoven, The Netherlands

Fire safety of buildings and structures is an important issue, and has a great impact on human life and economy. One of the processes negatively affecting the strength of a concrete building or structure during fire is spalling. Many examples exist in which spalling of concrete during fire has caused severe damage to structures, such as in the Mont Blanc and Channel Tunnel. Especially newly developed dense types of concrete such as HPC and SCC, have shown to be sensitive to spalling, hampering the application of these new concrete types. To reduce risks and building costs, the processes behind spalling need to be understood. Increasing our knowledge allows us to reliably predict the behaviour and take effective and cost friendly preventive measures. Moisture present in concrete is one of the reasons for spalling. When concrete is heated water will evaporate, which results in a high gas pressure inside the pores of concrete. This high gas pressure can induce spalling. To attain a better understanding of this process, a first step was taken to develop a finite element model (FEM) describing this transport of moisture in heated concrete. However, the validity of all current models (including our own) is unknown because of debatable input parameters and lack of experimental techniques to follow the transport process in situ. In cooperation with the Eindhoven University of Technology moisture transport in heated concrete can now be investigated with a home built dedicated 1D Magnetic Resonance Imaging (MRI) setup. Using the results of the MRI experiments the validity of our FEM models has been assessed for the first time. A general correspondence is observed. The FEM model described in this paper is a simplified FEM model compared to literature models. Already this simplified model shows a good correspondence with the MRI measurements.

*Key words: Concrete, spalling, NMR, MRI, moisture transport, fire, FEM, modelling*

# 1 Introduction

## 1.1 General introduction

Fire safety of buildings and structures is an important issue, and has a great impact on human life and economy. Authorities specify requirements on the fire safety of concrete structures, to guarantee the safety of users, rescue workers and other people in the vicinity of the structure. Furthermore authorities would like to reduce the costs due to possible damage, environmental effects or other properties. Also insurers demand safer and better prediction of the sustainability and safety of structures submitted to fire. Many examples exist in which spalling of concrete during fire has caused severe damage to structures, such as during the fires in the Mont Blanc and Channel tunnel. One of the processes that negatively affect the strength of such concrete building or structures is spalling. Fire in tunnels leads to high temperatures (over 1000 °C) and large temperature gradients, thereby feeding the two processes that drive spalling. First the high temperatures present inside the concrete leads to mechanical stresses, and second the free or hydrated water results in gas pressure build-up thereby introducing large stresses. Especially newly developed types of high performance concrete (HPC) have shown to be sensitive to spalling, hampering the application of these new concrete types.

Spalling of concrete under fire exposure is greatly dependent on its composite structure. The cement is a porous, hygroscopic material, the volume of which comprises of gel pores and capillary pores<sup>1</sup>. At room temperature the pores may be fully or partially filled with liquid water (l), water vapour (gw) and dry air (ga). Furthermore, water exists as physically bound water (adsorbed) or chemically bound water (hydrated water). When the concrete is heated, heat is transported through the concrete primarily by conduction. During this process of heating, the water present in the porous structure will be heated and starts to boil, resulting in an increasing gas-pressure. This pressure is the driving force for vapour transport out of the concrete and in addition will result in mechanical stresses and corresponding strains. Also chemical changes occur (e.g. dehydration) resulting in change in the mechanical properties in parallel. Both processes affect each other in the spalling process and results in a complex problem<sup>2</sup>.

To construct a model all these phenomena should be considered and evaluated. Despite the many challenges, difficulties, and uncertainties, many researchers have put a lot of effort in constructing a suitable model. This has led to several models available in literature, e.g. Bazant et al.<sup>3-5</sup>, Ahmed et al.<sup>6,7</sup>, Gawin et al.<sup>8-14</sup>, Schrefler<sup>15,16</sup>, and Davie<sup>17</sup>. The starting point for their work is based on less well known and less complex models for

coupled transport of heat and moisture in concrete by Tenchev et al. <sup>18-21</sup>, or Forsyth <sup>22</sup>. Simple transport models inside porous materials (e.g. in geosciences) hold also relevant information, see e.g. Hassizadeh <sup>23-27</sup>.

To our opinion the full complexity of the process can only be implemented in a meaningful model when subsequent steps are validated. Therefore, as a first step, the model used in this paper omits the effect of mechanical processes, and is limited to a coupling of moisture transport and heat transport. To validate our model a suitable technique is required, and was found in a new Magnetic Resonance Imaging (MRI) technique developed by the Eindhoven University of Technology <sup>28</sup>. This technique allows measuring moisture transport in heated concrete by using Nuclear Magnetic Resonance (NMR) as function of position and time, and was applied to several samples. In this paper simulations are compared with MRI results.

## 2 Theory and model

### 2.1 Moisture transport in heated concrete

Concrete is a porous material, which contains voids that are filled with air, water vapour and liquid water. To describe transport of moisture and heat the three phases, concrete (s), water (l), water vapour (gw) and air (ga), present in concrete have to be taken into account. By introducing the Representative Elementary Volume (REV) it is possible to describe the microscopic level by macroscopic variables. An important issue within the averaging theory is the size of the REV. The REV has to be small enough to be considered as infinitesimal, and at the same time must be large enough with respect to the heterogeneities of the material, to provide average quantities <sup>26</sup>. Figure 1 represents averaging of a three phase medium<sup>29</sup>.

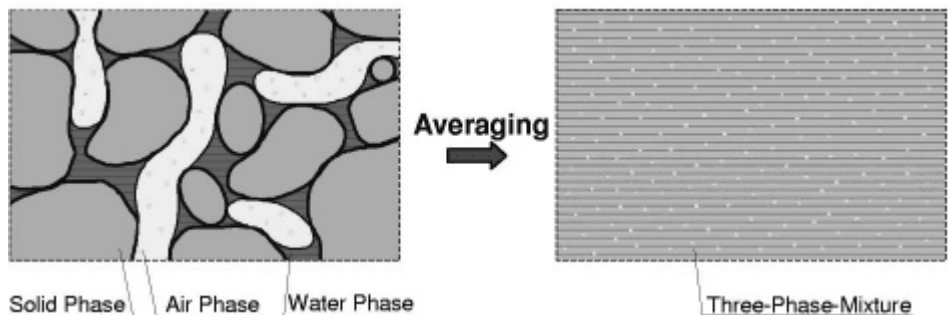


Figure 1: Averaging a three phase medium, left a Representative Elementary Volume (REV), right the average of a REV

After having applied the averaging theory a continuum description using differential equations may be used. In these differential equations the porosity of concrete is given by  $n$ . The pores are partly filled by liquid water and the water saturation of the pores is given by  $S$ , which means that  $(1-S)$  gives the fraction of gas, which consists of water vapour and air. In our model the densities are denoted by  $\rho_X$ , where  $X$  denotes the concrete phase (s), the water phase (l), the water vapour phase (gw) and air phase (ga), respectively. After applying a fire at the surface, densities and pressures will drive transport of water and gas. Three conservation equations for air, water, and energy form the basis of the model. The model is completed by inserting several laws that describe the thermodynamic state of water, the transport processes of the different constituents, and by inserting the necessary material properties. Finally, to be able to implement the model, suitable state variables have to be chosen.

## 2.2 *Simplifying the model using suitable assumptions*

To describe the process of spalling of concrete several assumptions have to be made to simplify the model and limit it to the major processes involved. The following list summarizes the assumptions made for the model in this paper.

- No change in porosity ( $n$ ) is assumed. The change of porosity by the dehydration process will affect the pore volume and the permeability; because the peak of the gas pressure should be located at temperatures much lower than 1000 °C (between 100 – 300 °C depending on the pressure), the increase in volume at the gas pressure peak will be small, due to a small change in porosity, and consequently will decrease the gas pressure only slightly. However, the induced change in permeability is of importance, but that effect is incorporated in the equations describing the permeability and does not require a change in the porosity variable ( $n$ ).
- Dehydration of concrete is an important source for water inside the pores, and is therefore included as a source term<sup>13,18</sup>.
- At high temperature diffusion of water vapour is no longer an important process<sup>30</sup>. At high temperatures moisture and water vapour transport is gas-pressure driven, and is diffusion is therefore not included in the model.
- Liquid water and water vapour are always in local equilibrium, so that the change in Gibbs free energy of liquid water and water vapour is always equal:  $dG_w = dG_{gw}$ . As a result the evaporation of water can be described by the Claudius-Clapeyron equation. Note that, assuming thermodynamic equilibrium also means that all materials in one

representative volume have equal temperatures and pressures. This assumption is, to our knowledge, used in all similar models described in literature.

- Heat capacity of gas is omitted in the effective capacity, since the heat capacity (density multiplied by the specific heat capacity) of gas is low compared to that of water and concrete. However, in case of convection the speed of the gas, and therefore the flux can be sufficiently high to be of relevance, so for convection of heat the heat capacity of the gas is included.
- Water is assumed to be incompressible, as a result the density of water is only a function of temperature.
- Influence of gravitation is neglected.

### 2.3 Conservation equations

To describe moisture and heat transport in concrete three conservation equations are used, for dry air, for water (including water vapour), and one for energy. To derive these equations several general conservation equations are used. For a conserved variable  $\psi$  (e.g. like mass, momentum and energy) the general conservation equation may be written as

$$\frac{\partial \psi}{\partial t} + \nabla \cdot J = H \quad (1)$$

with  $J = \psi v$  the transport flux and  $H$  the source or sink of  $\psi$ . In our model the conserved averaged variables are respectively:  $\psi \in \{(1-n)\rho_s, nS_w\rho_w, nS_g\rho_{ga}, nS_g\rho_{gw}, C_{eff}T\}$ , where  $n$  the porosity (between 0 and 1),  $S$  the saturation of the respective phase (sum of water and gas phase is 1) and  $C_{eff}$  the effective heat capacity of concrete and  $T$  the temperature. The subscripts denote the phase,  $s$  for solid matrix,  $w$  for water,  $ga$  air, and  $gw$  for water vapour.

After some mathematical substitutions three equations results, the water conservation law, which is a combination of (1) for water and water vapour,

$$\frac{\partial}{\partial t} (S_w\rho_w + S_g\rho_{gw}) + \nabla \cdot (S_w\rho_w v_w + S_g\rho_{gw} v_g) = \dot{\rho}_{hydr} \quad (2)$$

the dry air equation,

$$\frac{\partial (S_g\rho_{ga})}{\partial t} + \nabla \cdot (S_g\rho_{ga} v_g) = 0 \quad (3)$$

and the energy conservation equation,

$$C_{eff} \frac{\partial T}{\partial t} + (nS_w \rho_w c_w v_w + nS_g \rho_g c_g v_g) \cdot \nabla T - \nabla \cdot (\lambda_{eff} \nabla T) + \left\{ n \frac{\partial (S_g \rho_{gw})}{\partial t} + \nabla \cdot (nS_g \rho_{gw} v_g) \right\} \Delta H = 0 \quad (4)$$

Note that in Equation (2) only one term enters that describes the dehydration process, dehydration is a source for water, which disturbs the equilibrium that exists between water and water vapour. It is not relevant in which state the water is added, because in this model the equilibrium is reached instantaneously. However, in case of the energy equation, the shift in equilibrium will cause energy to be needed for the evaporation.

#### 2.4 Constitutive equations and material properties

Besides the conservation equations several material properties and state equations are required. A list of the required equations, which are explained in this paragraph: Clausius-Clapeyron equation (5), Kelvin equation (6), Darcy's law (for both water (7) and water vapour (8)), ideal gas law (9). Additionally, we require some material properties like: dehydration, water density as a function of temperature, permeability for different levels of saturation (for both water and water vapour), van Genugten equation (10)<sup>31</sup> (for the hydrodynamic potential). Each of these equations has its own limitation, introducing deviations in the model. However, at this time the goal is to see whether this model would describe the moisture transport accurately within the first order.

The Clausius-Clapeyron equation gives the vapour pressure as a function of temperature

32,33

$$p_{\infty}(T) = p_0 \cdot e^{-\frac{L}{R} \left( \frac{1}{T} - \frac{1}{T_{ref}} \right)}, \quad (5)$$

where  $p_0 = 101325$  Pa is the water vapour pressure at  $T_{ref} = 373$  K,  $L = 40.7$  kJ mol<sup>-1</sup> the enthalpy of vaporization,  $p_{\infty}$  is the water vapour pressure at a certain temperature  $T$  and  $R=8.314$  JK<sup>-1</sup>mol<sup>-1</sup> the gas constant. Inside a porous material the effective vapour pressure is lower due to capillary forces<sup>31,34,35</sup>. A meniscus in a pore causes the vapour pressure to decrease, because of a reduction in surface tension. If the radius of curvature of the meniscus increases the capillary pressure increases.

$$p_{gw}(p_c, T) = p_{\infty} \cdot e^{-\frac{p_c m_w}{\rho_w R T}}, \quad (6)$$

$p_c$  the capillary pressure,  $p_\infty$  the water vapour pressure,  $R = 8.314 \text{ JK}^{-1}\text{mol}^{-1}$  the gas constant, and  $m_w$  is molar mass of water in  $\text{kg/m}^3$ . The Clausius-Clapeyron equation and the Kelvin equation can be used to describe thermodynamic equilibrium between water and water vapour inside a porous materials, see also <sup>22,34,35</sup>.

Moisture transport in a porous material has three driving forces, the difference in gas pressure, the capillary forces (in case of water), and diffusion. As already discussed in the list of assumptions, diffusion is neglected as a driving force in the concrete spalling model. As a result of this assumption gas pressure and capillary pressure remains, which can be described by Darcy's law, eq. (7) and (8).

$$v_w = -\frac{K_w}{\mu_w} \frac{\partial}{\partial x} (p_g - p_c) \quad (7)$$

$$v_g \approx v_{ga} \approx v_{gw} = -\frac{K_{gw}}{\mu_{gw}} \frac{\partial}{\partial x} p_g \quad (8)$$

where  $\mu_w$  and  $\mu_{gw}$  represents the dynamic viscosity of water and water vapour, and  $K_w$  and  $K_{gw}$  the permeability of the concrete for liquid water and water vapour. Darcy's law applied for liquid water also contains capillary pressure, which is an additional driving force for liquid water. In our model the gas velocities of all components (water vapour, dry air or a mixture) are considered to be equal, and equal to that for water vapour.

To calculate gas pressure from the gas density inside a porous material we use the ideal gas law,

$$p = \bar{\rho}RT \quad (9)$$

where  $\bar{\rho}$  is the molar density of the gas,  $R$  the ideal gas constant, and  $T$  the temperature of the gas. The ideal gas law is not valid at pressures near the critical pressure of water  $0.1 p_c < p < p_c$ , the difference can go up to a factor of 5.

The van Genugten equation describes the saturation as a function of capillary pressure or hydrodynamic potential<sup>31</sup>. The saturation characteristic of a porous material can be fitted using the van Genugten equation:

$$S = \left( \frac{1}{(\alpha\Psi)^n + 1} \right)^{1-\frac{1}{n}}, n = 1.9 \quad (10)$$

where  $\alpha$  is a constant, and  $\Psi$  the hydrodynamic potential which can be replaced by  $\Psi = -p_c / (g \rho_w)$ .

### 2.5 FEM implementation

After rewriting, simplification and specifying the boundary conditions, the model was implemented in COMSOL 3.2. In principle the proposed material model can be applied to simulate multiple dimensions, however, only the 1D case was simulated because of the 1D character of the MRI experiments. The differential equations were solved for the three coupled variables,  $p_g$ ,  $p_c$ ,  $T$ .

The time dependent solver was used. Mesh size, time step and accuracy were varied to test the stability of the solution. The default element type - Lagrange Quadratic - was used. In Appendix A the applied element size and mesh size are specified. All high gradients in the response occurred at the heated left side of the model, therefore, mesh refinements were introduced at the left-hand side. In the final model the mesh refinements showed to be not necessary for a good solution. For the fired clay brick a total of 7.5 hours was computed with 15 minute time steps. For the concrete sample, 2 hours was computed with 5 minute time steps. An accuracy of  $1e-3$  (relative and absolute) was used in the simulations. It was observed that the numerical process does not converge when the saturation  $S$  is larger than 0.99. This can be related to the fact that the model is not valid for fully saturated situations when  $S$  is equal to 1.

## 3 Experimental setup for validation

### 3.1 Samples

Two concrete samples, were investigated by FEM and Magnetic Resonance Imaging (MRI). The concrete compositions of the two samples investigated are shown in table 3.1. Both samples were vacuum saturated before put into the MRI setup. In all experiments thermocouples were inserted into the sample, positioned at 5, 10, 15, 20, 30 mm from the heated surface.

### 3.2 MRI principles

Almost all nuclei have a magnetic dipole moment, resulting from their spin-angular momentum. (One can think of a nucleus as a charged sphere spinning around its axis, which corresponds to a current loop, generating a magnetic moment). In an Nuclear Magnetic Resonance (NMR) experiment the magnetic moments of the nuclei are manipulated by suitably chosen electromagnetic radio frequency (RF) fields. The frequency of the resonance conditions is given by,

$$f_l = \frac{\gamma}{2\pi} B_0, \quad (11)$$

where  $f_l$  is the so-called Larmor frequency [Hz],  $B_0$  [T] the externally applied static magnetic field and  $\gamma$  is the gyromagnetic ratio which is dependent on the type of nucleus (for 1H  $\gamma/2\pi = 42.58$  MHz T<sup>-1</sup>). Because of this condition the method can be made sensitive to only hydrogen and therefore to water. When a known magnetic field gradient is applied, the constant magnetic field  $B_0$  in the resonance condition (Eq. 1) has to be replaced by the spatially varying magnetic field,

$$B(x) = B_0 + Gx, \quad (12)$$

where  $G$  [T m<sup>-1</sup>] (Fig. 2) is the magnetic field gradient and  $x$  is the position of the precessing magnetic moment. The resonance condition is then spatially dependent. Therefore the moisture content at different positions  $x$  in the sample can be measured by varying the resonance frequency without moving the sample.

In a pulsed NMR experiment the orientation of the moments of the spins are manipulated by short RF pulses at the resonance frequency. The amplitude of the resulting signal emitted by the nuclear spins, the so-called 'Hahn spin-echo' <sup>36</sup> signal is proportional to the number of nuclei taking part in the experiment. The spin-echo signal also gives information about the rate at which this magnetic excitation of the spins decays. The system will return to its magnetic equilibrium by two mechanisms: interactions between the nuclei themselves, causing the so-called spin-spin relaxation (characterized by a  $T_2$  value), and interactions between the nuclei and their environment, causing the so-called spin-lattice relaxation (characterized by a  $T_1$  value). In principle the signal decay can be related to the pore size distribution, and it is expected that changes in the pore size distribution by dehydration at elevated temperatures can be followed by NMR.

Table 3.1: Sample characteristics

Concrete characteristics	A (only MRI)	C (MRI and FEM)
Intended $f_{cc}$ [MPa]	90	90
Slump [mm]	50-80	50-80
<b>Mixture Properties</b>		
CEM I 52.5 R [kg/m <sup>3</sup> ]	430	450
Granite [kg/m <sup>3</sup> ]	1202	1210
Washed grit sand [kg/m <sup>3</sup> ]	709	680
Glenium 51 [kg/m <sup>3</sup> ]	4.73	4.95
PP 18 x 6 - 165 [kg/m <sup>3</sup> ]		2
Water [kg/m <sup>3</sup> ]	129	135
Actual w/c ratio [-]	0.3	0.3

### 3.3 MRI setup

For the experiments described in this study, a home built NMR scanner is used. This instrument was designed for quantitative measurements of moisture in porous materials with short transverse relaxation ( $T_2$ ) times (unlike standard MRI, which is generally used in a qualitative way). The machine makes use of the magnet of a whole body MRI scanner (Gyrosan, Philips) which operates at a main field of 1.5 T corresponding to a frequency of 63.9 MHz (Fig. 1). The setup is placed within the scanner and a schematic diagram is given in Figure 2. Two Helmholtz coils provide the magnetic field gradient  $G$  in the direction of  $B_0$ . The magnitude of the gradient is  $100 \text{ mT m}^{-1}$ , providing a spatial resolution of the order of 2 mm. A home built birdcage coil is used for applying the RF pulses, and receiving the NMR signal from the sample. The coil is 60 mm long and has a diameter of 60 mm. A birdcage coil is used because it generates a homogeneous  $B_1$ -field perpendicular to the sample. Therefore, the coil can be placed parallel to the main magnetic field providing optimal use of the available space inside the bore. The sample is heated with a halogen lamp. The reflector of the lamp was gold plated to ensure maximum reflection of the infra-red radiation. The sample is placed inside the birdcage coil and is thermally insulated using mineral wool in order to create a 1D experiment<sup>28</sup>.



Figure 2: The magnet of the medical-imaging machine used in the spalling experiments and the experiment set-up used

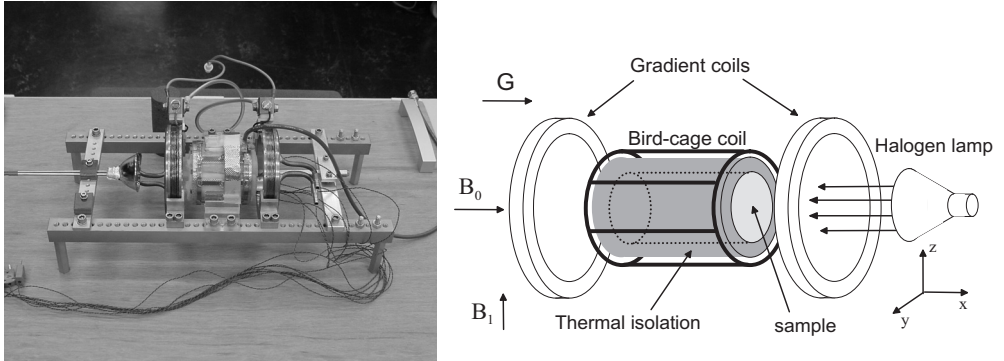


Figure 3: Left a picture of the NMR insert on the right a schematic diagram of the NMR setup. The helmholtz coil configuration provide a gradient  $G$  of  $100 \text{ mT m}^{-1}$ . A bird-cage coil is used for the reception and transmission of RF pulses. A halogen lamp is used to heat the sample.

## 4 Results of simulations and MRI measurements

### 4.1 Yellow fired-clay brick

In Figure 4 the saturation profiles measured with NMR for fired-clay brick are shown every 15 minutes for a total of 7.5 hours. Initially the sample is fully saturated, so the first profile corresponds to  $S = 1$ . Note that this is not the case for the simulation shown in Figure 5. For specific details about the model parameters, see also Appendix A.1. The current implemented model cannot correctly calculate the behaviour of moisture transport near saturation level 1. To overcome this problem saturation in the model was set at 0.9. After 1.5 hours a clear drying front develops. From 0 - 1.5 hours the moisture profiles are more homogeneous. In Figure 5 simulations are shown for the fired clay brick. A general correspondence is seen between the saturation profiles and the simulation profiles. The homogeneous drying, in the beginning of the drying experiment, is due to the capillary forces inside the fired clay brick. In the experiment when the saturation equals approximately 0.4, the signal at the right side of the front starts to drop less fast. In the simulations this effect is not as pronounced.

The temperatures measured by the 8 thermocouples are shown in Figure 6, with thermocouples positioned every 5 mm, and the first 5 mm from the surface. Please note the inflection at 50 min, this is due to a heating problem in the beginning of the experiment. At  $100 \text{ }^\circ\text{C}$  a change in curvature can be seen, corresponding to the boiling of water inside the pores. The temperatures obtained from the simulation are shown in Figure 7. It can be seen that the experiment and the simulations correspond rather well, except that the boiling

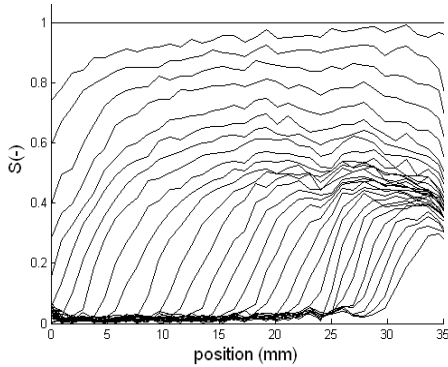


Figure 4: Saturation profiles for the fired-clay brick. The profiles are shown every 15 minutes for a total of 7.5 hours. The first profile is normalised at  $S=1$ . A clear drying front develops after 1.5 hours.

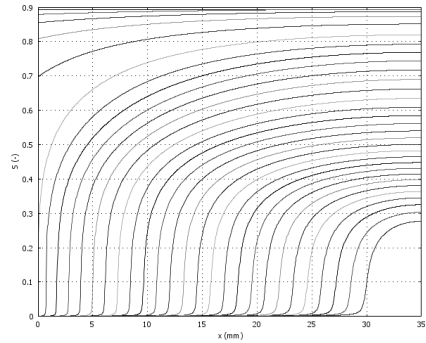


Figure 5: Simulation profiles for the fired-clay brick. The profiles are shown every 15 minutes for a total of 7.5 hours.

temperature in the simulation is higher approximately  $125\text{ }^{\circ}\text{C}$  due to the higher gas pressure. This can be attributed to the fact that the drilled holes, in which the thermocouples are inserted, allow the gas to escape. The total amount of water inside the brick as a function of time is calculated from the MRI profiles and is shown in Figure 8. Figure 9 shows the integral of the simulation. One can clearly see that initially in the simulation the decrease of signal is lower. The most probable reason is that the temperature in the experiment at the surface was higher or increased faster compared to the simulations. A best guess was used for the temperature of the surface in the simulations.

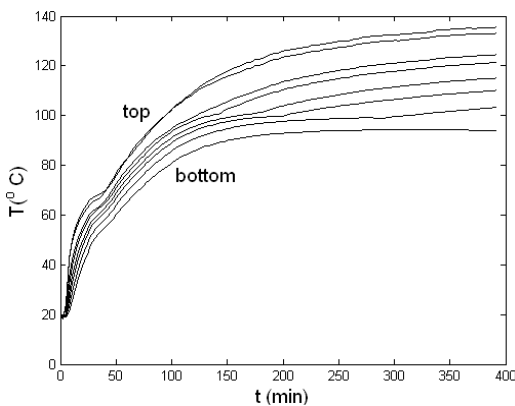


Figure 6: Temperature as a function of time at different positions in the brick sample. The highest temperatures correspond to the thermocouples close to the surface.

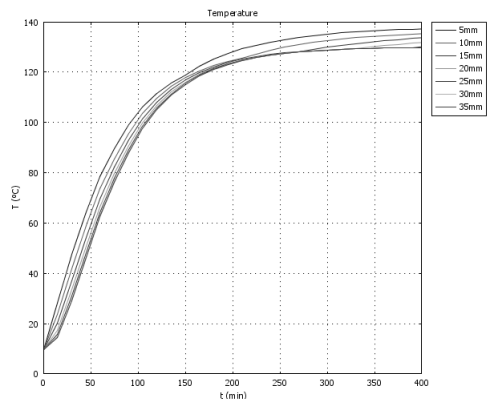


Figure 7: Simulation profiles for the fired-clay brick. The profiles are shown every 15 minutes for a total of 7.5 hours.

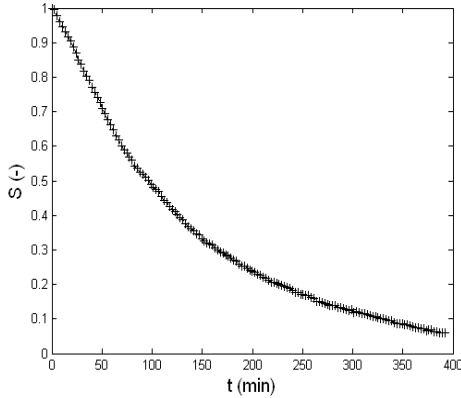


Figure 8: Total water content as a function of time

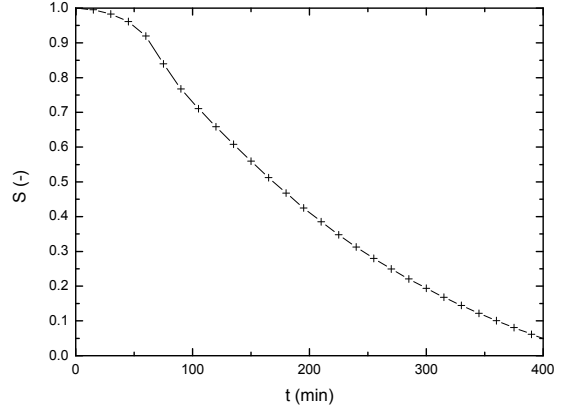


Figure 9: Simulation of the total water content as a function of time

As the sample is heated, an evaporation front becomes visible (according to Figure 6 at 100 °C), and moves through the sample. In Figure 10 the location 100 °C inside the sample and the drying front are plotted. In this figure, it is clear that the drying front (which is equal to the evaporation front) moves slower than the 100 °C position, which indicates an increased gas pressure inside the fired clay brick. Boiling is actually taking place at a higher temperature, which corresponds to the simulations, which shown that the boiling point was approximately 125 °C. In the experiment the gas pressure at the location of the thermocouple is equal to the gas pressure outside the sample, because the drilled holes allowed the gas to escape. The gas pressure inside the samples, determined from the simulations, is plotted in Figure 11. Note that in this picture the gas pressure is constant behind the boiling front.

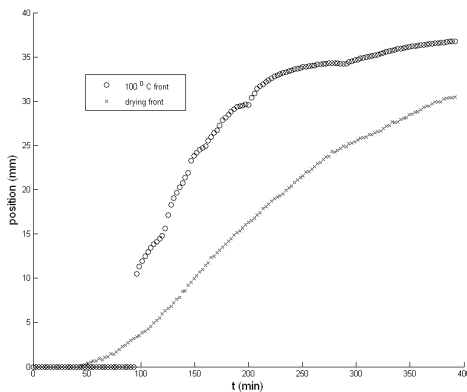


Figure 10: Positions of both the drying front (x) and the 100 °C front

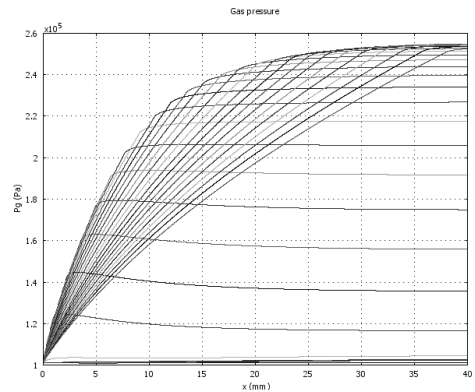


Figure 11: Gas pressure as a function of position inside the fired clay brick. Note that the gas pressure is 2.6 times the atmospheric pressure.

#### 4.2 Concrete sample A

The profiles of this sample are shown in Figure 12. The results show a peak, which is a consequence of background signals, in this case radio signals. The amount of water present is too low to follow the process with sufficient spatial and time resolution. However, from the profiles we can still observe that the sample is homogeneously drying. This homogeneous drying indicates that the evaporation at the surface is slower than the transport of water to the surface by capillary forces and/or diffusion. This observation is strengthened by Figure 13, which shows a relatively low surface temperature of max 200 °C after 2 hours. For a porous system, such as a fired clay brick, this temperature is high enough, however, for concrete it is not. The pores of concrete are much smaller than for fired clay brick, leading to high capillary forces that drive water transport. As a consequence the transport of water to the surface is higher than the amount of water vapour that is generated at the surface by evaporation. Therefore at no time in this experiment a drying front detaching from the surface is observed. Our model is only valid when the gas pressure of the water vapour is higher than the internal capillary forces. Consequently simulating these results using our model is not possible. Higher temperatures at the surface are required. In Figure 13 we see the temperature measured by thermocouples. In Figure 14 the moisture content of the whole sample is plotted. The moisture content decreases as a function of time due to evaporation of water caused by heating of the sample at the surface.

#### 4.3 Concrete sample C containing poly-propylene fibers

In Figure 15 moisture profiles measured by MRI are presented, which show a gradient in the moisture content. In this concrete sample polypropylene fibers were added which melt

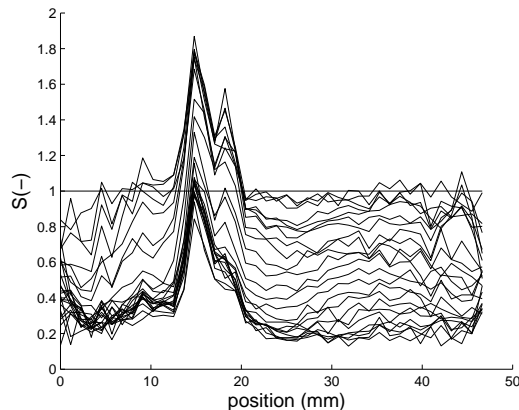


Figure 12: Moisture profiles sample A. Profiles given are every 6.5 min.

at approximately 165 °C. The profiles correspond rather well to the simulated profiles shown in Figure 16. For specific details about the model parameters, see also Appendix A.2.

In Figure 17 the measured temperature is plotted at different positions: 5, 10, 15, 20, 30 mm from the surface. In Figure 18 the temperature of the simulations is plotted at different positions. Note that in this Figure 17 the temperature remains constant at 100 °C for a short period, indicating that boiling is occurring at that position. In fact the boiling takes place at a higher temperature, as in case of the fired-clay brick, the high gas pressure can escape from the sample in the experiment via the drilled holes. Note that the same temperature is reached after 100 min for all thermocouples, which is not observed in the MRI experiment (Fig. 17). This difference can be explained by the fact that in the simulation the sample is ideally insulation, which is not the case in the NMR experiments.

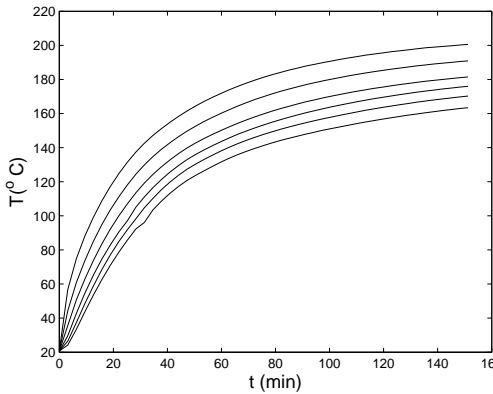


Figure 13: Temperature of sample A

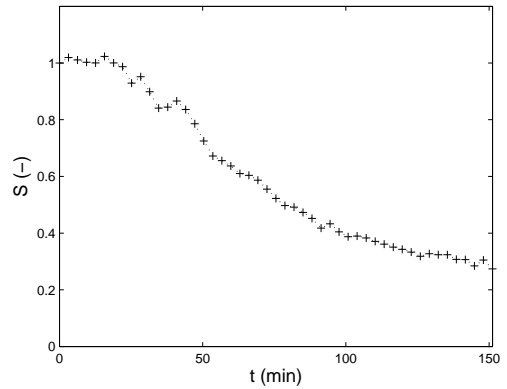


Figure 14: Total moisture content of sample A

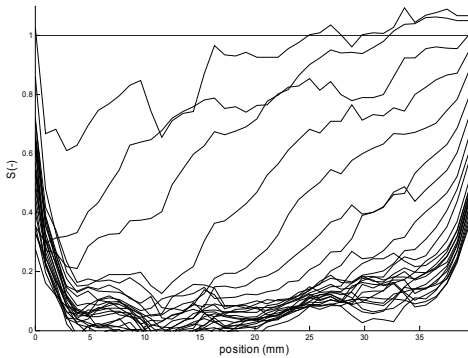


Figure 15: Moisture profiles of concrete sample. Profiles are given every 5 min.

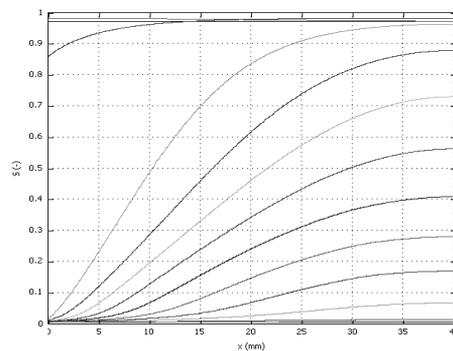


Figure 16: Moisture profiles of concrete sample. Profiles are given every 5 min.

The overall signal intensity of the sample is calculated, the final signal level which is reached is due to the background noise. In the simulations presented in Figure 20 background noise is not present. After about 50 minutes in both the measurements and the simulation the moisture content has reached a constant level. This indicates that the simulation is corresponding rather well to the experiment.

## 5 Conclusions and discussion

In first order the global features observed in the simulations correspond to those observed in the MRI experiments. However, several differences are observed. For instance the temperatures in the simulations with respect to the boiling of water do not correspond to the temperatures measured in the experiment. The boiling in the simulations takes place at

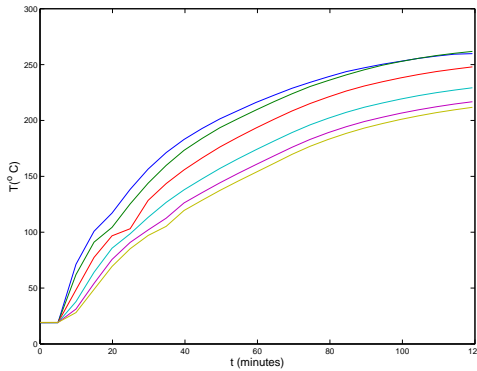


Figure 1: Temperature, at 5, 10, 15, 20, 25, 30 mm of sample C

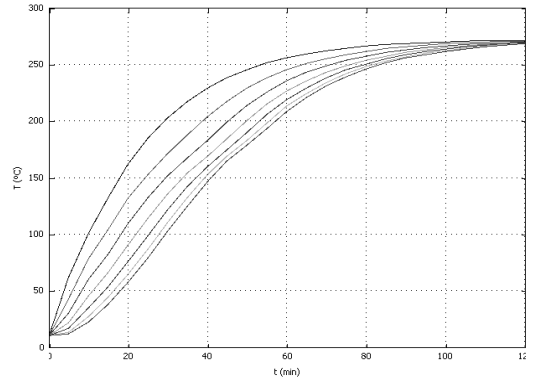


Figure 2: Temperature, at 0, 5, 10, 15, 20, 25, 30 mm of sample C

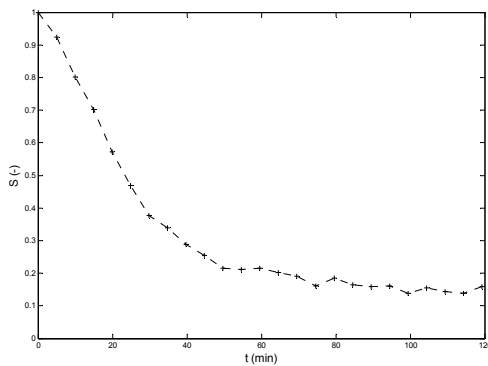


Figure 3: Total moisture content of sample C

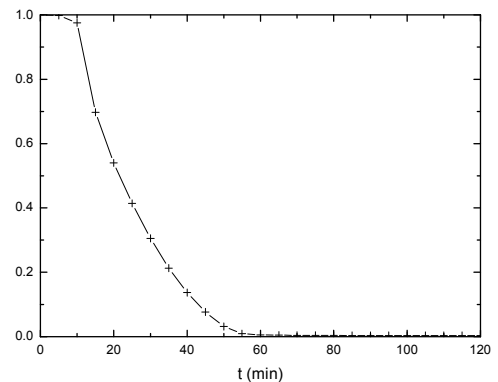


Figure 4: Simulated moisture content of sample C

125 °C and in the experiment at 100 °C. This can be explained by the fact that gas can escape from the drilled holes, allowing the gas pressure in the sample to equilibrate with atmospheric pressure.

Another difference between simulations and experiments is the final temperature that is reached. In the simulations the temperatures at different depths reach the same value. However, in the MRI experiment different final temperatures are reached, the difference is caused by heat loss to the environment from the walls of the sample, which is not the case for the 1D simulations.

The model cannot correctly predict moisture transport behaviour when full saturation is reached. At full saturation the gas pressure on the fully saturated pores is transferred via the water phase. Water will be forced into the unsaturated pores behind the fully saturated region. If the whole sample is saturated, moisture will bleed from the back side of the sample. However, both instances were not incorporated in the current model, and therefore the model cannot accurately describe moisture clogging and bleeding.

In all simulations the input parameters describing the material properties were a best guess and were then optimized for the best correspondence between experiment and simulation. Further research should not only focus on optimizing the simulations, but also on determining the most relevant material properties, such as permeability, porosity, dehydration, permeability for water and water vapour as a function of temperature and saturation. Additionally in a next step interaction between moisture transport and mechanical behaviour should be investigated. All these future steps require subsequent validation, in which MRI as a validation tool has proven to be very valuable.

To validate the model at high temperatures the MRI setup has still to be improved to be able to measure at these high temperatures. Additionally the size of the sample is still rather small. At this moment the Eindhoven University of Technology is working on both these improvements.

### *Acknowledgements*

The authors wish to thank Jaap Feijen and Jef Noijen for the construction of the NMR setup. Part of this research was supported by the Dutch Technology Foundation (STW), and TNO Built Environment and Geosciences.

## Literature

- [1] A. M. Neville, *Properties of concrete* London, ed. 2nd, (1973).
- [2] A. K. Gabriel, *Progress in Structural Engineering and Materials* 2, 429-447 (2000).
- [3] Z. P. Bazant, J. C. Chern, W. Thonguthai, *Nuclear Engineering and Design* 68, 61-70 (1982).
- [4] Z. P. Bazant, *American Ceramic Society Bulletin* 60, 369 (1981).
- [5] Z. P. Bazant and W. Thonguthai, *Journal of the Engineering Mechanics Division-ASCE* 104, 1059-1079 (1978).
- [6] G. N. Ahmed and J. P. Hurst, *Fire Technology* 35, 232-262 (1999).
- [7] G. N. Ahmed and C. L. D. Huang, *Chemical Engineering Communications* 91, 241-253 (1990).
- [8] D. Gawin, C. Alonso, C. Andrade, C. E. Majorana, F. Pesavento, *Computers and Concrete* 2, 189-202 (2005).
- [9] D. Gawin, *Computers and Concrete* 2, 203-214 (2005).
- [10] D. Gawin, F. Pesavento, B. A. Schrefler, *Materials and Structures* 37, 218-236 (2004).
- [11] D. Gawin, F. Pesavento, B. A. Schrefler, *Computer Methods in Applied Mechanics and Engineering* 192, 1731-1771 (2003).
- [12] D. Gawin, M. Lefik, B. A. Schrefler, *International Journal for Numerical Methods in Engineering* 50, 299-323 (2001).
- [13] D. Gawin, C. E. Majorana, B. A. Schrefler, *Mechanics of Cohesive-Frictional Materials* 4, 37-74 (1999).
- [14] D. Gawin and B. A. Schrefler, *Engineering Computations* 13, 113-& (1996).
- [15] B. A. Schrefler, G. A. Khoury, D. Gawin, C. E. Majorana, *Engineering Computations* 19, 787-819 (2002).
- [16] B. A. Schrefler, P. Brunello, D. Gawin, C. E. Majorana, F. Pesavento, *Computational Mechanics* 29, 43-51 (2002).
- [17] C. T. Davie, C. J. Pearce, N. Bicanic, *Numerical Heat Transfer Part A-Applications* 49, 733-763 (2006).
- [18] L. Y. Li, J. A. Purkiss, R. T. Tenchev, *Proceedings of the Institution of Mechanical Engineers Part C-Journal of Mechanical Engineering Science* 216, 213-224 (2002).
- [19] R. Tenchev and P. Purnell, *International Journal of Solids and Structures* 42, 6550-6565 (2005).

- [20] R. T. Tenchev, L. Y. Li, J. A. Purkiss, *Numerical Heat Transfer Part A-Applications* 39, 685-710 (2001).
- [21] R. T. Tenchev, L. Y. Li, J. A. Purkiss, B. H. Khalafallah, *Magazine of Concrete Research* 53, 117-125 (2001).
- [22] P. A. Forsyth and R. B. Simpson, *International Journal for Numerical Methods in Fluids* 12, 655-682 (1991).
- [23] S. M. Hassanizadeh, *Advances in Water Resources* 9, 196-206 (1986).
- [24] S. M. Hassanizadeh, *Advances in Water Resources* 9, 207-222 (1986).
- [25] S. M. Hassanizadeh and W. G. Gray, *Advances in Water Resources* 3, 25-40 (1980).
- [26] S. M. Hassanizadeh and W. G. Gray, *Advances in Water Resources* 2, 131-144 (1979).
- [27] S. M. Hassanizadeh and W. G. Gray, *Advances in Water Resources* 2, 191-203 (1979).
- [28] G. H. A. van der Heijden, R. M. W. Bijnen, L. Pel, H. P. Huinink, *Cement and Concrete Research* 37, 894-901 (2007).
- [29] M. Shamalta, J. Fellingner, A. Breunese, "Numerical modelling of the spalling of concrete due to high temperature" 2006).
- [30] Y. Ichikawa and G. L. England, *Nuclear Engineering and Design* 228, 245-259 (2004).
- [31] C. Hall and W. D. Hoff, *Water transport in brick, stone and concrete* (Spon Press, ed. 1, 2002).
- [32] D. V. Schroeder, *An introduction to thermal physics* (Addison Wesley Longman, 2000).
- [33] W. Greiner, L. Neise, H. Stocker, *Thermodynamics and statistical mechanics* (Springer-Verlag New York, 1995).
- [34] J. G. Powles, *Journal of Physics A-Mathematical and General* 18, 1551-1560 (1985).
- [35] L. M. Skinner and J. R. Sambles, *Aerosol Science* 3, 199-210 (2007).
- [36] E. L. Hahn, *Physical Review* 80, 580 (1950).

## Appendix A

### A.1 Model parameters for the fired clay brick

#### Relevant constants in model

Name	Value	Description
$J_s$	1.67	Heat conductivity dry concrete (W/Km)
$J_w$	0.6	Heat conductivity water (W/Km)
$C_s$	940	Heat capacity concrete (J/kgK)
$C_w$	4200	Heat capacity water (J/kgK)
$C_g$	2000	Heat capacity gas (J/kgK)
$n$	0.3	Porosity brick (-)
$L$	40700	Evaporation Enthalpy (J/mol)
$\rho_s$	2680	Density brick (kg/m <sup>2</sup> )
$K_0$	2.5e-15	Initial permeability (m <sup>2</sup> )
$K_{wr0}$	0.8	Relative water permeability (normally a function of $S, T$ )
$K_{gr0}$	0.5	Relative vapor permeability (normally a function of $S, T$ )
$m$	1.9	Coefficient needed for $S(P_c, T)$
$P_{c0}$	1e4	Initial capillary pressure (Pa)
$\rho_w$	1e3	Water density (kg/m <sup>3</sup> )

#### Relevant scalar expressions

Name	Expression	Description
$P_{gw0}$	$P_0 \cdot \exp(-(L/R) \cdot (1/T - 1/373))$	Clausius-Clapeyron equation
$P_{gw}$	$P_{gw0} \cdot \exp(-(P_c \cdot M_w) / (R \cdot T \cdot \rho_w))$	Kelvin Equation
$K_g$	$K_0 \cdot K_{gr0} \cdot (1-S)^4$	Permeability gas
$K_w$	$K_0 \cdot K_{wr0} \cdot S^4$	Permeability water
$C_{eff}$	$(1-n) \cdot \rho_s \cdot C_s + n \cdot \rho_w \cdot C_w \cdot S$	Effective heat capacity
$J_{eff}$	$(1-n) \cdot J_s + n \cdot S \cdot J_w$	Effective heat flux
$S$	$((1 + (5e-5 \cdot P_c)^m)^{-(1-1/m)})$	Saturation as a function of capillary force (m see constants)
$T_i$	$283 + 130 \cdot (1 - \exp(-t/(100 \cdot 40)))$	Surface temperature

#### Mesh size and parameters

Maximum element size	1e-4
Number of degrees of freedom	2103
Number of elements	350

## A.2 Model parameters for concrete sample C

### Relevant constants in model

Name	Value	Description
$J_s$	1.67	Heat conductivity dry concrete (W/Km)
$J_w$	0.6	Heat conductivity water (W/Km)
$C_s$	940	Heat capacity concrete (J/kgK)
$C_w$	4200	Heat capacity water (J/kgK)
$C_g$	2000	Heat capacity gas (J/kgK)
$n$	0.13	Porosity concrete (-)
$L$	40700	Evaporation Enthalpy (J/mol)
$\rho_s$	2680	Density concrete (kg/m <sup>3</sup> )
$K_0$	5e-17	Initial permeability (m <sup>2</sup> )
$K_{wr}$	1	Relative water permeability (normally a function of $S, T$ )
$K_{gr}$	20	Relative vapor permeability (normally a function of $S, T$ )
$m$	1.9	Coefficient needed for $S(P_c, T)$
$P_{c0}$	0.5e6	Initial capillary pressure (Pa)
$\rho_w$	1e3	Water density (kg/m <sup>3</sup> )

### Relevant scalar expressions

Name	Expression	Description
$P_{gw0}$	$P_0 \cdot \exp(-(L/R) \cdot (1/T - 1/373))$	Clausius-Clapeyron equation
$P_{gw}$	$P_{gw0} \cdot \exp(-(P_c \cdot M_w) / (R \cdot T \cdot \rho_w))$	Kelvin equation
$K_g$	$K_0 \cdot K_{gr} \cdot (1-S)^4$	Permeability gas
$K_w$	$K_0 \cdot K_{wr} \cdot S^4$	Permeability water
$C_{eff}$	$(1-n) \cdot \rho_s \cdot C_s + n \cdot \rho_w \cdot C_w \cdot S$	Effective heat capacity
$J_{eff}$	$(1-n) \cdot J_s + n \cdot S \cdot J_w$	Effective heat flux
$S$	$((1 + (5e-7 \cdot P_c)^m)^{-1} - (1-1/m))$	Saturation as a function of capillary force (m see constants)
$T_i$	$283 + 262 \cdot (1 - \exp(-t / (20 \cdot 60)))$	Surface temperature

### Mesh size and parameters

Maximum element size	0.5e-3
Number of degrees of freedom	483
Number of elements	80

### A.3 Differences between two simulations

In the table below the difference between the two simulations are specified.

Name	Value Brick	Value concrete	Description
$n$	0.3	0.13	Porosity concrete (-)
$Kwr$	0.8	1	Relative water permeability (normally a function of $S, T$ )
$Kgr$	0.5	20	Relative vapor permeability (normally a function of $S, T$ )
$K0$	2.5e-15	5e-17	Initial permeability (m <sup>2</sup> )
$Pc0$	1e4	0.5e6	Initial capillary pressure (Pa)
$S$	$((1+(5e-5*Pc)^m)^{-1-1/m})$	$((1+(5e-7*Pc)^m)^{-1-1/m})$	Saturation as a function of capillary force (m see constants)
$Ti$	$283+130*(1-\exp(-t/(100*40)))$	$283+262*(1-\exp(-t/(20*60)))$	Surface temperature

Note that the permeability has a very strong dependence on the saturation level. This high dependence gave the best correspondence with the measured data, normally a smaller dependence is used in literature;  $Kw \sim S^n$ , where  $1 \leq n \leq 3$ . The boundaries at the right side of the sample were closed.  $Ti$  describes the temperature profile at the left boundary.